J Mater Sci (2008) 43:7013–7025
DOI 10.1007/s10853-008-3042-y

Microstructure and phase stability in a Nb–Mo–Cr–Al–Si alloy

**Yan-Ling Hu · Alexandre L. Vasiliev ·
Lichun Zhang · Kai Song · Mark Aindow**

Received: 26 September 2008 / Accepted: 7 October 2008 / Published online: 30 October 2008

Abstract The microstructures in as-cast and heat-treated samples of an Nb–27Mo–27Cr–9Al–9Si (in at.%) alloy have been investigated using X-ray diffraction and electron microscopy techniques. The as-cast alloy comprises a dendritic A2 solid solution surrounded by a eutectic mixture of A15 and C14 phases. After heat treatment at 1,000 °C, there is extensive precipitation of A15 and C15 phases within the A2 dendrites, while the A15/C14 eutectic remains essentially unchanged. After heat treatment at 1,500 °C, the precipitates within the A2 phase exhibit the A15 and C14 structures; these are coarser and more equiaxed than those formed at 1,000 °C, and there is also extensive coarsening/spheroidization of the A15/C14 eutectic. Small particles of two unknown phases were also observed within the A2 dendrites in the heat-treated samples. The orientation relationships between the phases have been identified and these are used to deduce the way in which the microstructure develops.

Introduction

There has been a concerted effort to identify structural materials that can be used in very high-temperature environments. In gas turbine engines, for example, replacing Ni-based superalloys with higher melting point materials could result in more efficient engine designs. Ordered intermetallic compounds based upon aluminides of Ti and Ni have received extensive attention, but only offer relatively modest increases in the range of operating temperatures over the Ni-based superalloys [1–3]. Intermetallic compounds based on the refractory transition metals would seem to be the most promising candidate materials for very high-temperature environments, and the compounds that have been considered include those with the A15 structure (e.g. Nb_3Al [4–7]), Laves phases (e.g. Cr_2Nb [8–11]), 5–3 silicides (e.g. Mo_5Si_3[12, 13]), etc. The common problem with these compounds is that they all exhibit low-fracture toughness under ambient conditions in the monolithic form.

One approach that can be used to ameliorate the low toughness of such refractory intermetallics is to form composite materials that incorporate a ductile toughening phase. The most straightforward way of doing this is to exploit peritectic or eutectic reactions to form “in situ composites” by solidification of alloy melts with appropriate chemical compositions [14–17]. Examples of ductile-phase-toughened composites produced in this manner include combinations of body-centered-cubic (BCC) solid solutions with: A15 phases (Cr–Cr_3Si [18, 19], V–V_3Si [20], Nb–Nb_3Al [21–24]), Laves phases (Nb–Cr_2Nb [25–27], Cr–Cr_2Nb [27–29], Cr–Cr_2Zr [29], (Ti,Cr)–Cr_2Ti [30], Cr–Cr_2(Zr,Nb) [31, 32], Cr–Cr_2(Zr,Hf) [31, 32], Cr–Cr_2Ta [33–35]), and 5–3 silicides (Nb–Nb_5Si_3 [36–41], Mo–Mo_3Si–Mo_5SiB_2 [42–44]).

Y.-L. Hu · A. L. Vasiliev · L. C. Zhang · K. Song ·
M. Aindow (✉)
Materials Science and Engineering Program, Department
of Chemical Materials and Biomolecular Engineering, Institute
of Materials Science, University of Connecticut, 97 North
Eagleville Road, Storrs, CT 06269-3136, USA
e-mail: m.aindow@uconn.edu

Present Address:
A. L. Vasiliev
Institute of Crystallography, Russian Academy of Sciences,
Leninskij pr., 59, Moscow, Russia

Present Address:
K. Song
Department of Materials Science and Engineering,
Lehigh University, Bethlehem, PA 18015, USA

Of these composites, the ones that contain Cr_2X Laves phases (where X = Ti, Zr, Hf, Nb, or Ta) are particularly attractive for high-temperature structural applications, because the Laves phases have high melting points, relatively low densities and good oxidation resistance. Moreover, the Cr_2X Laves phases can accommodate significant amounts of various ternary transition metal additions in solid solution, and so there is the potential to modify the properties of these phases by alloying [27–35]. For example, balanced properties of 20 MPa $m^{1/2}$ for room-temperature fracture toughness and 350 MPa for yield strength at 1,000 °C have been reported for a Cr–30Fe–6.3Ta–4Mo–0.5Ti–0.3Si–0.1La (at.%) alloy with a Cr–Cr_2Ta-type eutectic structure [45].

In the present study, we have performed a detailed microstructural evaluation of a quinternary alloy with the nominal composition Nb–27Mo–27Cr–9Al–9Si (at.%), which was first reported by Shah et al. [14]. This alloy was selected because it is based upon the Nb–Cr_2Nb system, which has been identified previously as being well suited to the aero-engine environment [25–27]. Moreover, the high Mo content of the alloy should lead to strengthening of the ductile phase and a lowering of the ductile-to-brittle transition temperature (DBTT) of the Cr_2Nb Laves phase, thereby increasing the toughness of the composite at ambient temperature [46]. The main drawback of the high Mo content is that this can compromise the oxidation resistance, but the addition of Al and Si may compensate for this and should stabilize the Laves phase [47]. We note that Shah et al. found no evidence for catastrophic oxidation in this alloy after 48 h at 1,371 °C in air [14]. In this paper we present data on the crystal structures, morphologies and orientation relationships exhibited by the phases in this alloy in the as-cast and heat-treated conditions. The details of site occupancies and the roles that these play in the mechanical behavior of the constituent phases are presented in a separate paper [48].

Experimental procedure

A lens-shaped button of the alloy designated NbX-9101 by Shah et al. (nominal composition Nb–27Mo–27Cr–9Al–9Si in at.%) was produced by arc-melting in a water-cooled copper hearth [14]. Portions of the as-cast button were wrapped in Ta foil and encapsulated under vacuum in quartz tubes. The encapsulated samples were heat-treated in a tube furnace at 1,000 °C and 1,500 °C for times of up to 200 h, and then cooled slowly to room temperature in the furnace. No evidence for oxide scale formation was noted on any of the heat-treated samples indicating that the gettering of O by Ta was effective.

The microstructures exhibited by the as-cast and heat-treated specimens were characterized using X-ray diffraction (XRD), scanning electron microscopy (SEM), and transmission electron microscopy (TEM). For the samples heat-treated at 1,500 °C the microstructure was rather coarser than for the other samples; this made TEM specimen preparation more challenging and so phase identification was performed using a combination of electron back-scattered diffraction (EBSD) and TEM for these samples.

Samples for SEM and EBSD experiments were prepared by mechanical grinding, coarse polishing with 3 μm diamond slurry, then fine polishing with 0.05 μm colloidal silica. Some of the SEM samples were etched electrochemically to give better contrast between the phases in secondary electron (SE) images. This electrochemical etching was performed using a mixture of 5% $HClO_4$ and 5%H_2SO_4 in methanol at −20 °C with an applied voltage of 15 V. SE images were obtained in a JEOL JSM-6335F field-emission SEM, whereas EBSD and energy dispersive X-ray spectrometry (EDXS) experiments were performed in a Hitachi S-3200H SEM equipped with a HKL Nordlys EBSD detector and an EDAX EDXS detector.

TEM specimen blanks were prepared by cutting 3 mm diameter disks from the samples using electro-discharge machining (EDM), then grinding and polishing to a thickness of less than 150 μm. Final thinning was performed by twin-jet electro-polishing to perforation using a mixture of 5% $HClO_4$ and 5%H_2SO_4 in methanol at −40 °C with an applied voltage of 15 V. Where necessary, site-specific TEM specimens were prepared using focused ion beam (FIB) sectioning in an FEI Strata DB235 dual-beam FIB/SEM.

Diffraction contrast images and diffraction patterns were acquired in a Philips EM420 TEM operating at an accelerating voltage of 120 kV. High-resolution TEM (HRTEM) phase contrast lattice images and EDXS spectra were obtained in a JEOL JEM-2010 TEM equipped with a UHR objective lens pole-piece ($C_s \approx 0.5$ mm), operating at an accelerating voltage of 200 kV, and equipped with an EDAX Phoenix atmospheric thin window EDXS system.

To avoid the effects of texture in the samples, X-ray powder diffractometry was used to identify the phases and to measure their lattice parameters. Portions of each specimen were cooled to well below the DBTT using liquid nitrogen and these were then crushed to a fine powder. X-Ray diffraction (XRD) spectra were obtained from the powders using a Bruker-AXS D5005 X-Ray diffractometer with a Cu Kα source ($\lambda = 0.15406$ nm). The lattice parameters of the structures were extrapolated from the peak positions using the Nelson-Riley and Cohen methods [49].

Results

Microstructure of the as-cast alloy

The SE images obtained from the as-cast samples in the SEM revealed the presence of coarse primary dendrites with a fine interdendritic eutectic mixture. One such image is shown in Fig. 1. By analyzing many such images it was found that the mean volume fraction of the primary dendritic phase is $\approx 30\%$ whereas the eutectic comprises roughly equal proportions of the constituent phases. Selected area diffraction patterns (SADPs) obtained from TEM samples of the as-cast microstructure revealed that the dendrites exhibit the A2 (body-centered cubic) structure, and that the eutectic is a mixture of a cubic A15 phase and a hexagonal C14 Laves phase. The lattice parameters obtained for these phases using XRD are: A2—$a_0 = 0.315$ nm; A15—$a_0 = 0.496$ nm; C14—$a_0 = 0.497$ nm, $c_0 = 0.811$ nm. The compositions measured using EDXS in the TEM from Nb, Mo L-peaks, and Cr, Al, Si K-peaks are given in Table 1.

Bright field (BF) TEM images such as Fig. 2a obtained from the A2 dendrites revealed a very low defect density in this phase. The only defects observed were dislocations arranged into very-low-angle boundaries delineating subgrains of around 1 μm in diameter. SADPs obtained from this phase with the beam direction, **B**, parallel to <110> exhibited diffuse intensity between the A2 reflections, as shown in the inset to Fig. 2a. This indicates the development of some short-range order (SRO) in the A2 phase. No evidence for coring of these dendrites was observed.

The interdendritic A15/C14 eutectic mixture adopts a predominantly lamellar morphology, with a mean interlamellar spacing of ≈ 0.3 μm. While many of the lamellae appear to be curved in the SE SEM images, BF TEM images such as Fig. 2b show that the A15/C14 interfaces are locally planar, and the microscopic curvature corresponds to combinations of different planar interfacial facets. This suggests that there is significant anisotropy in the interface energy (e.g. [50]). The TEM images also reveal the presence of planar faults in both phases: those in the A15 phase lie parallel to $\{100\}$, whereas those in the C14 phase lie on (0001), $\{1\bar{1}00\}$ and $\{1\bar{1}01\}$ planes. The faults are more common in the vicinity of facet junctions on the A15/C14 interfaces than elsewhere.

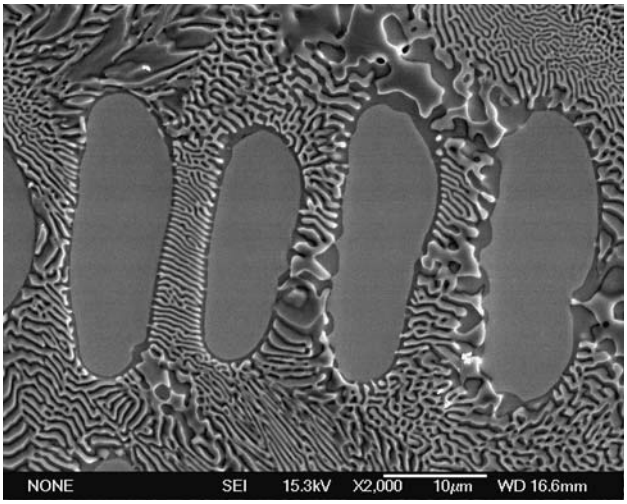

Fig. 1 SE SEM micrograph showing the overall microstructure of the as-cast sample

Table 1 Compositions of the phases in the as-cast microstructure

Phase	Composition (at.%)				
	Nb	Mo	Cr	Al	Si
A2	30.7	43.3	16.8	7.2	2.0
A15	29.4	34.9	15.9	10.9	8.9
C14	29.1	13.1	40.0	6.2	11.6

The orientation relationships (ORs) between the A15 and C14 phases in the eutectic were determined by analyzing SADPs obtained from different eutectic colonies. Once symmetry-equivalent variants had been eliminated, four crystallographically distinct ORs were identified:

OR1: $[001]_{A15}//[\bar{2}20\bar{3}]_{C14}$, $(\bar{1}3\bar{5})_{A15}//(0001)_{C14}$
OR2: $[001]_{A15}//[\bar{2}20\bar{3}]_{C14}$, $(\bar{2}35)_{A15}//(0001)_{C14}$
OR3: $[001]_{A15}//[\bar{1}2\bar{1}0]_{C14}$, $(\bar{3}10)_{A15}//(0001)_{C14}$
OR4: $[001]_{A15}//[\bar{2}20\bar{3}]_{C14}$, $(\bar{1}12)_{A15}//(0001)_{C14}$

Examples of the SADPs obtained from each of these ORs are presented in Fig. 3.

In almost all cases, the primary A2 dendrites were encased in a layer of the A15 phase (Fig. 1). In some cases, however, a very thin strip of Laves phases was found between the A2 dendrite and the A15 layer (Fig. 4a). Variations in contrast were observed within this strip and microdiffraction patterns such as Fig. 4b and c obtained from such regions reveal that parts of the strip exhibit the cubic C15 structure, rather than the hexagonal C14 structure adopted by the other Laves phase regions in the as-cast microstructure. The C15 strips from which sufficient diffraction data could be obtained exhibited the OR:

OR5: $[1\bar{1}0]_{C15}//[010]_{A15}$, $(001)_{C15}//(001)_{A15}$

Microstructure of samples heat-treated at 1,000 °C

For the samples heat-treated at 1,000 °C, SE SEM images such as Fig. 5 show no significant change in the morphology of the phases from that observed for the as-cast samples, but the contrast within the primary dendrites is rather different. The BF TEM images obtained from the

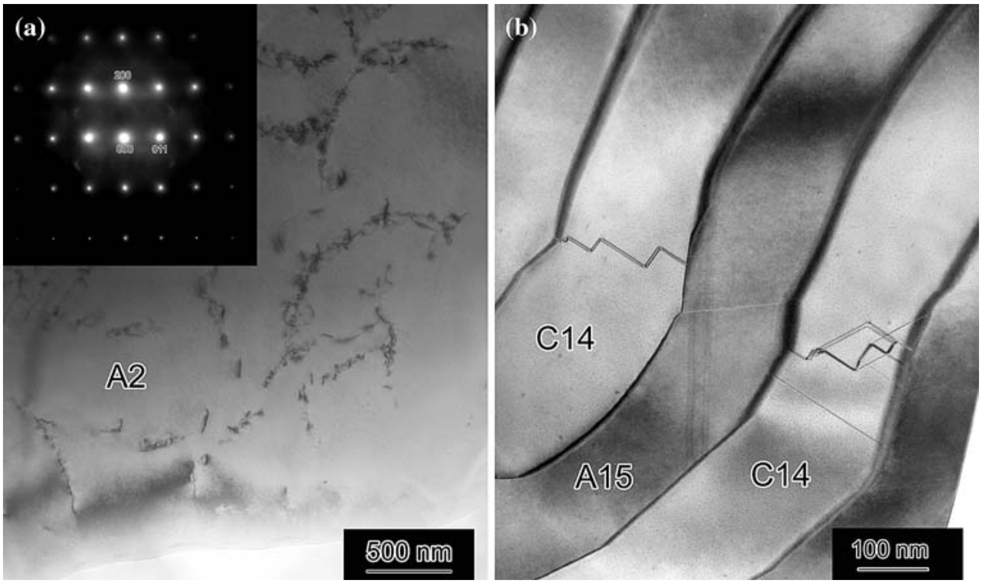

Fig. 2 TEM data from the as-cast alloy: **a** dislocations within the primary A2 solid solution, the inset SADP shows short range ordering; **b** stacking faults within the A15/C14 eutectic

Fig. 3 SADPs showing the four distinct ORs found for A15/C14 eutectic colonies in the as-cast sample: **a** OR1, $\mathbf{B} = [\bar{1}3\bar{2}]_{A15}//[1\bar{1}00]_{C14}$, **b** OR2, $\mathbf{B} = [1\bar{1}1]_{A15}//[0\bar{1}10]_{C14}$, **c** OR3, $\mathbf{B} = [13\bar{2}]_{A15}//[11\bar{2}0]_{C14}$, and **d** OR4, $\mathbf{B} = [1\bar{1}1]_{A15}//[0\bar{1}10]_{C14}$

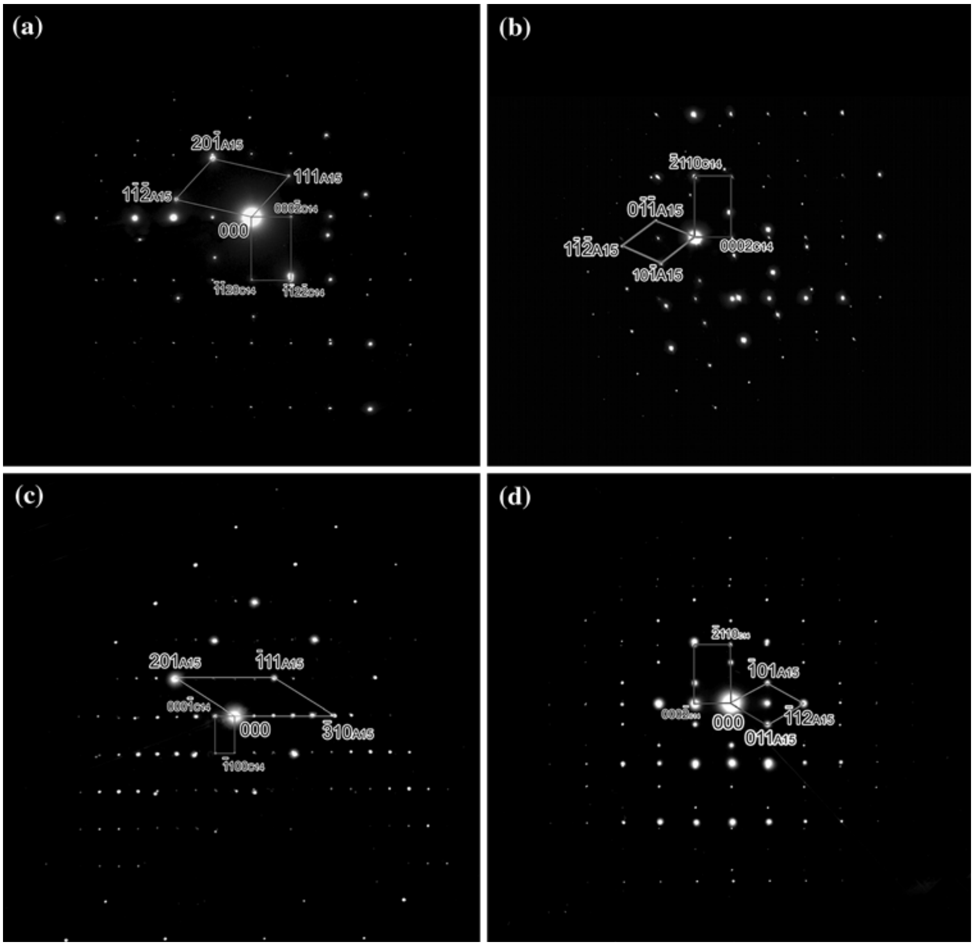

dendrites show that this change in contrast corresponds to the formation of a high density of precipitates within the A2 phase (Fig. 6a, b). There are two distinct types of precipitates present: lath-like particles, 0.5–3 μm in length and ≈100 nm in thickness; and ellipsoidal particles of up to 100 nm in diameter. We note that the precipitates are

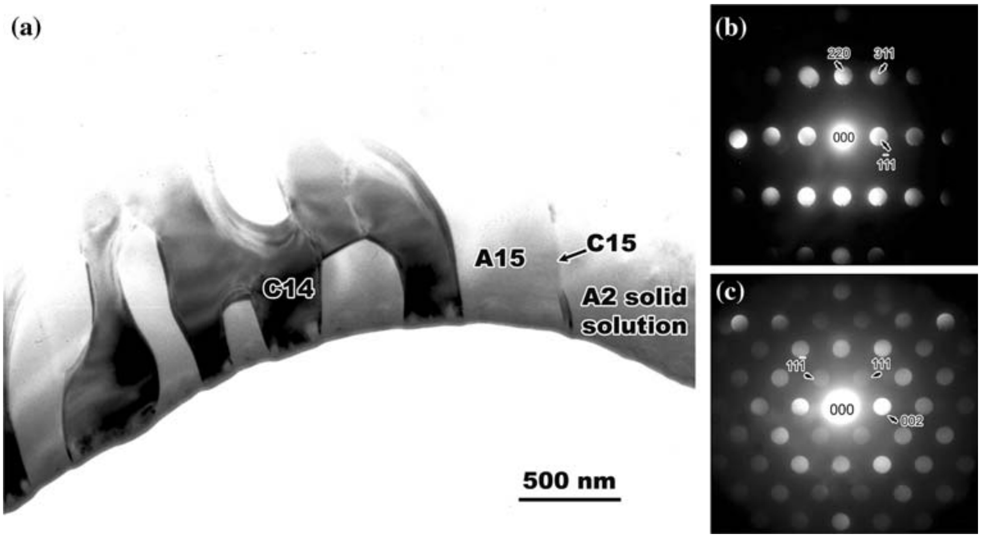

Fig. 4 TEM data from the as-cast alloy: **a** BF TEM image of the boundary between an A15/C14 eutectic colony and an A2 dendrite; microdiffraction patterns obtained from the narrow strip of Laves phase between the A15 lamella and the A2 dendrite in (**a**) showing that the strip exhibits the cubic C15 structure—(**b**) **B** = $[\bar{2}11]_{C15}$ and **c B** = $[\bar{1}10]_{C15}$

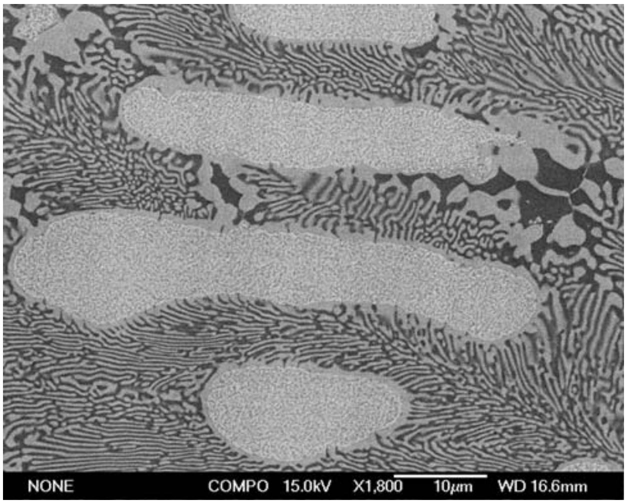

Fig. 5 Back-scattered electron SEM micrograph showing the overall microstructure of the sample heat-treated at 1,000 °C for 100 h

distributed uniformly throughout the dendrites confirming the absence of coring effects and that this precipitation is accompanied by the disappearance of the diffuse SRO intensity in SADPs from the A2 phase.

Higher-magnification images obtained from the lath-like precipitates (e.g. Fig. 7a) reveal a composite structure with a central core surrounded by a sheath 10–20 nm in thickness. The crystallography of these particles was investigated using HRTEM imaging and SADPs: examples are shown in Fig. 7b, and in Fig. 7c and d, respectively. It was found that the core exhibits the A15 structure whereas the sheath has the cubic C15 structure. Both phases are oriented with {001} parallel to the habit plane of the particle, i.e. parallel to the main A15/C15 interface. In most cases (e.g. Fig. 7c) the OR across this interface was OR5 (i.e. the same as for the thin C15 strips at the A15/A2 interface as shown in Fig. 4). Occasionally, a different OR was observed in such composite laths, as shown in Fig. 7d:

OR6: $[\bar{1}30]_{C15}//[\bar{1}20]_{A15}$, $(001)_{C15}//(001)_{A15}$

Both of the phases in these laths were faulted. The A15 cores contained stacking faults on {100} and one example is indicated in Fig. 7b. From the projected displacements we deduce that the displacement vector $\mathbf{R} = (a_0/4)\langle 021\rangle$, which is consistent with that observed elsewhere [51] in intermetallic phases with the A15 structure. The C15 phases contained much higher densities of defects with both {111}<112> twins and stacking faults lying on {111}. It is interesting to note that the ORs adopted by the lath-like precipitates with respect to the surrounding A2 phase are less well-defined but these usually lie within a few degrees of:

OR7: $[110]_{A2}//[001]_{A15}$, $(\bar{1}10)_{A2}//(210)_{A15}$ or
OR8: $[110]_{A2}//[1\overline{21}]_{A15}$, $(\bar{1}10)_{A2}//(210)_{A15}$

The ellipsoidal precipitates were also found to exhibit the C15 Laves phase structure (Fig. 8a). As for the C15 sheath on the composite laths, some of the C15 ellipsoids contained micro-twins and stacking faults on {111}. An analysis of SADPs such as Fig. 8b obtained from the ellipsoidal precipitates revealed that, unlike the laths, these ellipsoids exhibit a singular OR with respect to the surrounding A2 phase:

OR9: $[11\bar{1}]_{C15}//[\bar{2}11]_{A2}$, $(1\bar{1}0)_{C15}\hat{}(\bar{1}1\bar{3})_{A2} = 1.4°$

We note that some of the Laves phase particles that lay at the edge of the hole in the TEM samples exhibited very different defect structures, with extremely high densities of twins and faults lying parallel to a particular habit plane. A particularly clear example of this is shown in Fig. 8c, wherein a Laves phase particle protrudes into the hole and

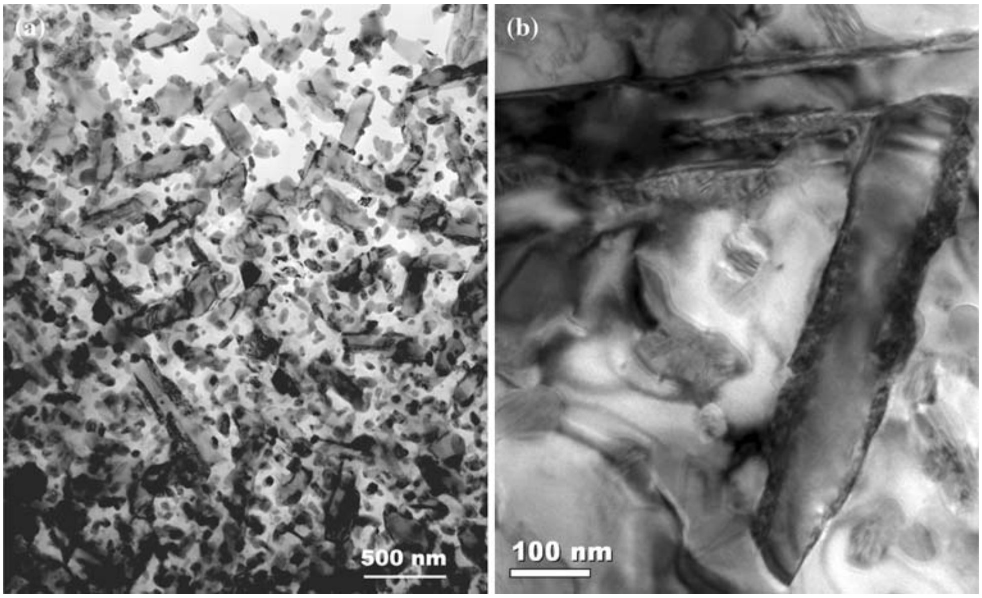

Fig. 6 BF TEM images showing the precipitates formed within the primary A2 solid solution for the sample heat-treated at 1,000 °C for 100 h

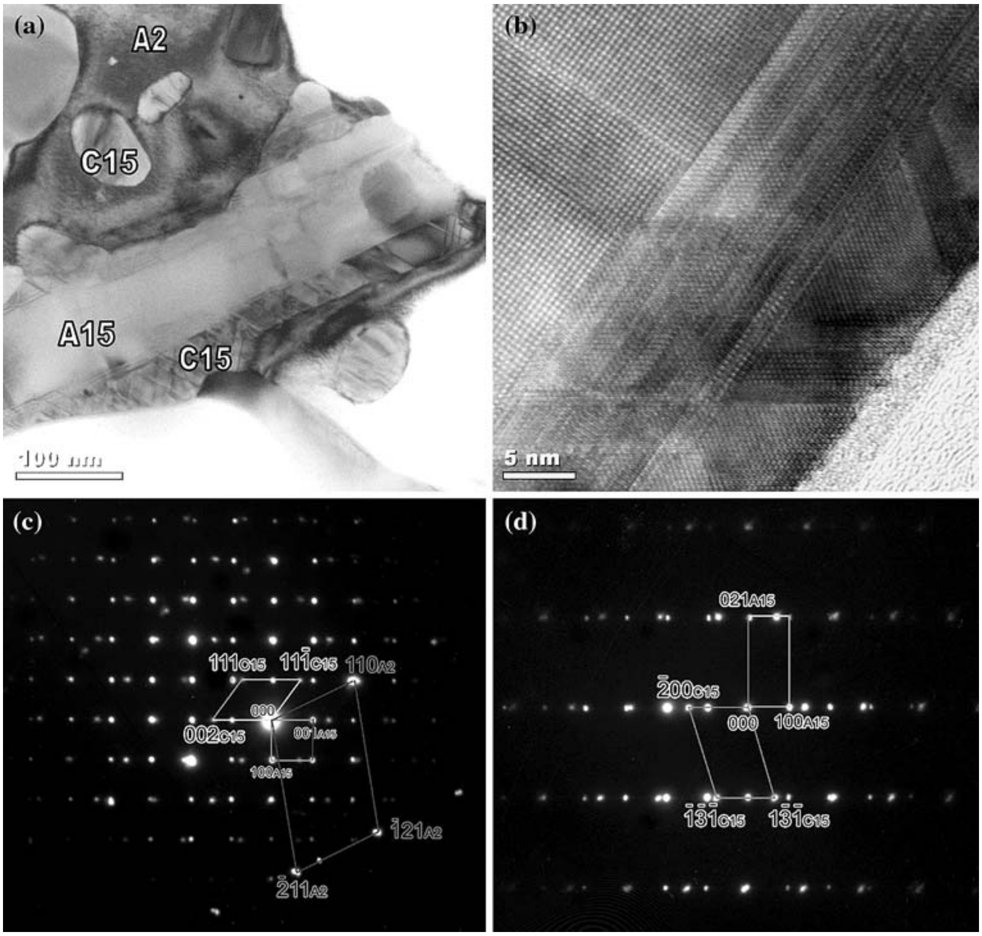

Fig. 7 TEM data from the sample heat-treated at 1,000 °C for 100 h: **a** BF TEM image of an A15/C15 composite lath within the A2 solid solution; **b** HRTEM image showing stacking faults within the A15 core and the C15 sheath of a composite lath; SADPs showing the two distinct ORs found for the C15 sheath with respect to the A15 core in such laths—(**c**) OR5, $\mathbf{B} = [1\bar{1}0]_{C15}//[010]_{A15}$ and (**d**) OR6, $\mathbf{B} = [0\bar{1}3]_{C15}//[0\bar{1}2]_{A15}$

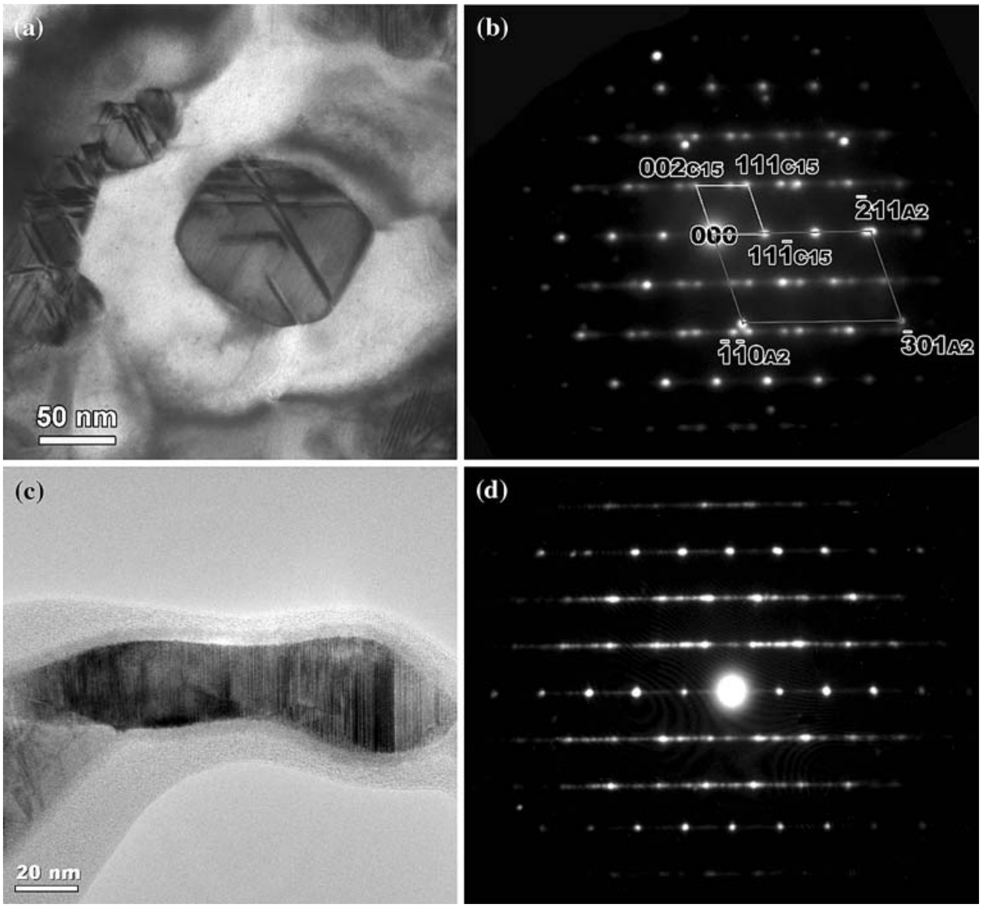

Fig. 8 TEM data from the sample heat-treated at 1,000 °C for 100 h: **a** BF TEM image of an ellipsoidal C15 precipitate within the A2 solid solution; **b** SADP showing the OR between the C15 ellipsoids and the A2 solid solution; **c** BF TEM image of a C15 precipitate at the edge of the hole in the TEM sample, containing a high density of parallel stacking faults on {111}; **d** SADP obtained with **B** = $[110]_{C15}$, showing streaks along 111

almost all of the surrounding A2 phase (and, indeed, some of the precipitate itself) has been removed during final thinning. There is a very high density of planar features oriented vertically in this image and the corresponding SADP (Fig. 8d) exhibits diffraction maxima corresponding to the hexagonal C14 and C36 Laves structures, in addition to those for the twinned C15 structure observed in Fig. 8b. The orientations of the C14 and C36 maxima in such patterns is consistent with what one would expect for a partial shear polymorphic transformation on a particular {111} in the C15 structure.

Occasional examples of a third type of precipitate were observed in the sample heat-treated at 1,000 °C for 200 h, as shown in Fig. 9a. These also adopted an ellipsoidal morphology, but in this case the diffraction maxima in the microdiffraction patterns and SADPs (Fig. 9b–e) were consistent with a face-centered-cubic lattice with $a_0 \approx$ 1.14 nm. There is no known cubic phase in the Nb/Mo/Cr/Al/Si system with such a large lattice parameter, but we note that Kumar and Liu [28] reported the formation of a cubic phase with $a_0 = 1.15$ nm in Cr–Cr_2Nb. In the latter case this was ascribed to an M_6C-type carbide, but the C content of the precipitates in the samples studied here is too low for this. This third type of precipitate was observed more frequently in the sample heat-treated at 1,000 °C for 200 h. Further work is underway to identify these precipitates.

The compositions of the various phases measured using EDXS in the TEM are given in Table 2. We note that there was no measurable increase in the oxygen signal for these spectra over those obtained from the as-cast alloy samples.

Microstructure of samples heat-treated at 1,500 °C

Much more significant microstructural changes were observed in the samples heat-treated at 1,500 °C (e.g. Fig. 10): the A15/C14 eutectic had undergone severe coarsening/spheroidization; the thickness of the A15 layer around the primary A2 phase was much greater; and the precipitates within the A2 phase were much coarser and

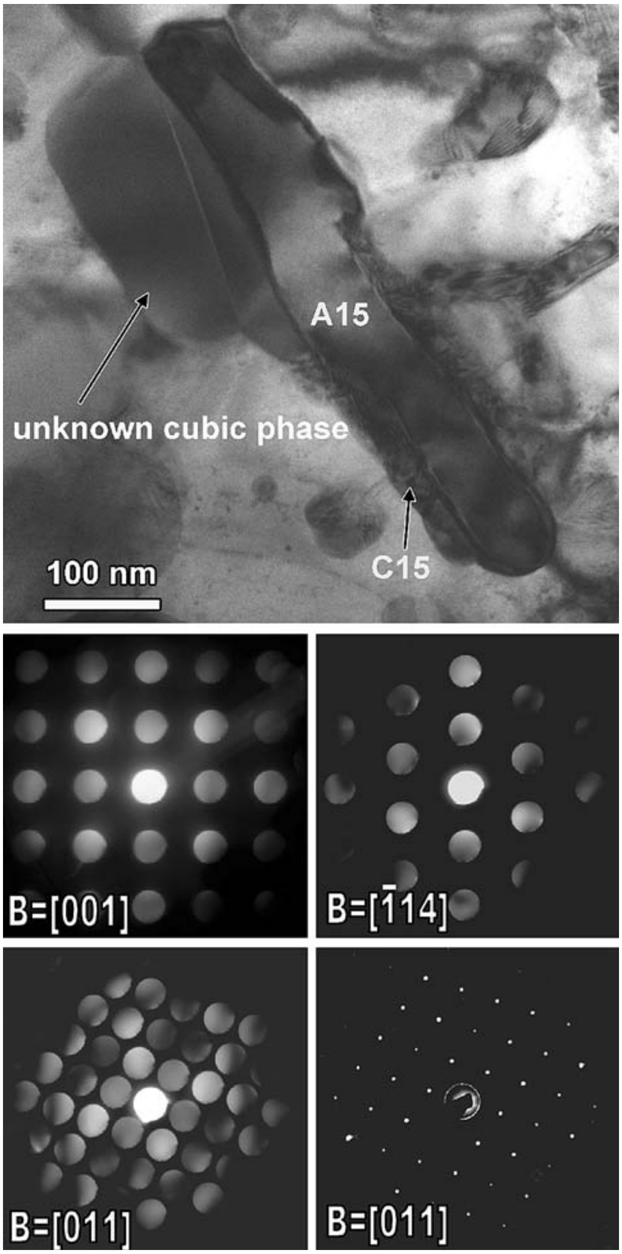

Fig. 9 TEM data from the sample heat-treated at 1,000 °C for 200 h: **a** BF TEM image showing ellipsoidal precipitates of an unknown phase within the A2 solid solution; **b**–**d** microdiffraction patterns; and **e** SADP showing a f.c.c lattice with $a_0 \approx 1.14$ nm

Table 2 Compositions of the phases in the microstructure after heat treatment at 1,000 °C

Phase	Composition (at.%)				
	Nb	Mo	Cr	Al	Si
A2	29.8	50.2	12.1	6.4	1.5
A15 (eutectic)	28.9	36.0	15.5	11.9	8.6
A15 (within A2)	25.6	41.1	10.4	21.1	1.8
C14 (eutectic)	30.5	10.0	43.8	3.7	12.0
C15 (sheath)	32.0	9.1	42.6	8.7	7.4
C15 (ellipsoids)	31.9	9.1	43.1	8.1	7.8
Unknown phase (I)	48.8	6.7	26.7	14.0	3.8

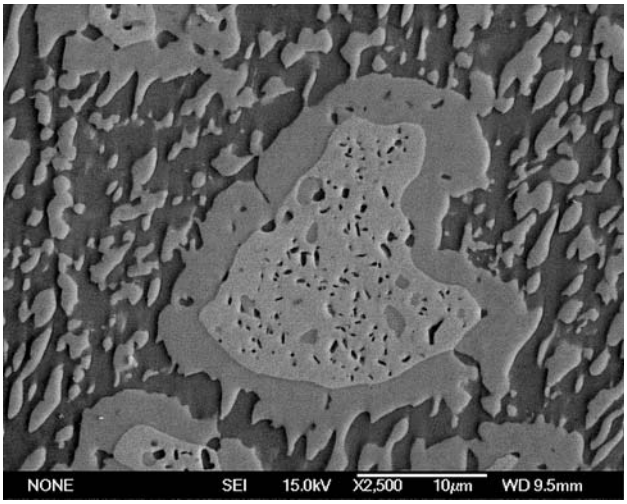

Fig. 10 SE SEM micrograph showing the overall microstructure of the sample heat-treated at 1,500 °C for 200 h

more equi-axed. Due to the scale of the microstructure it was necessary to use a combination of EBSD in the SEM and SADPs in the TEM to identify the phases unambiguously.

Here again, the largest precipitates exhibited the A15 structure and the ORs adopted with respect to the surrounding A2 phase lie within a few degrees of OR7 and OR8; in this case, however, there was no evidence of a Laves phase sheath around the precipitates. Most of the other precipitates exhibited the C14 structure, and an analysis of SADPs such as Fig. 11a–c revealed that the precipitates exhibited three crystallographically distinct ORs with respect to the A2 phase:

OR10: $[1\bar{1}00]_{C14}//[11\bar{1}]_{A2}$, $(0001)_{C14}//(101)_{A2}$
OR11: $[11\bar{2}0]_{C14}//[111]_{A2}$, $(0001)_{C14}//(\bar{2}11)_{A2}$
OR12: $[11\bar{2}0]_{C14}//[1\bar{1}3]_{A2}$, $(0001)_{C14}//(141)_{A2}$

A few particles were observed with a very different chemistry and crystal structure from those of the A15 and C14 precipitates. The EDXS data from these particles showed that they are very Al-rich (>90 at.% Al) but the zone axis SADPs obtained from these particles did not match those expected for any known aluminide phase of Nb, Mo, and/or Cr, or indeed with any other aluminide phase of which the authors are aware. Here again, further work is underway to identify the structure of this phase.

The compositions of the various phases measured using EDXS in the TEM are given in Table 3. Here again, no evidence for oxygen pick-up was observed. We note that, unlike the phases in the samples heat-treated at 1,000 °C, there are no significant differences in composition between

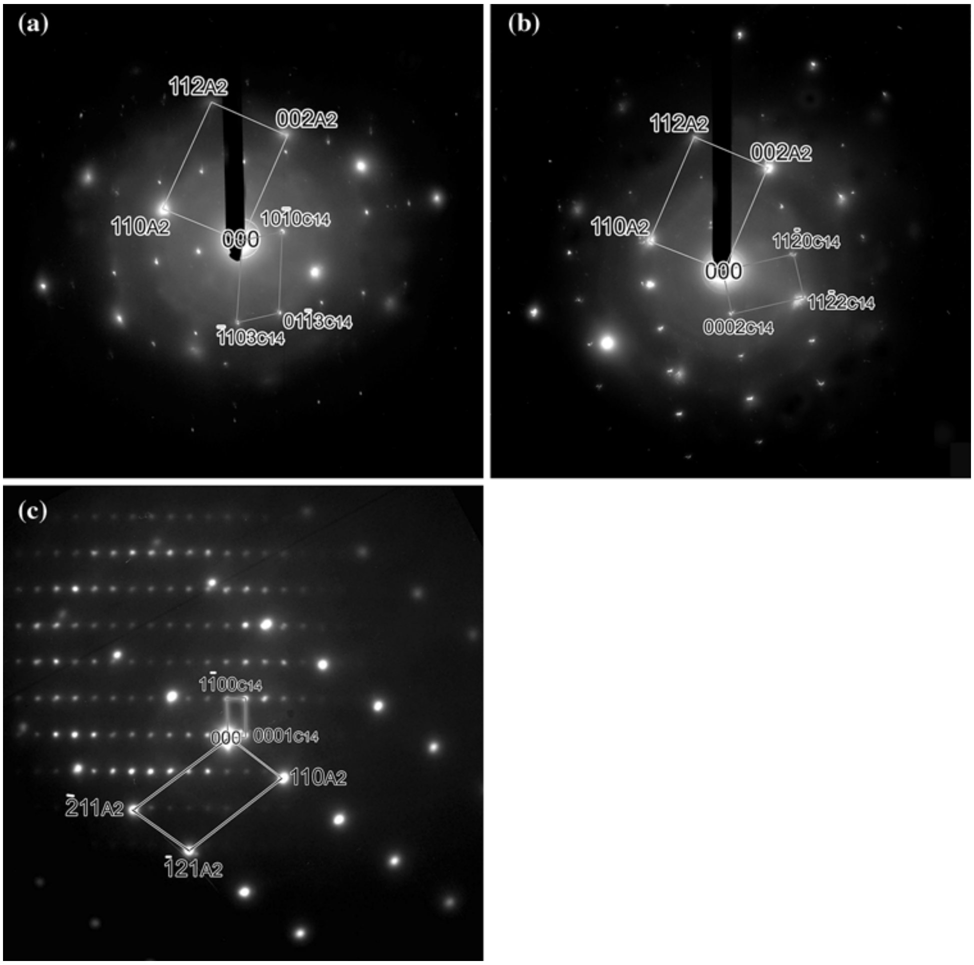

Fig. 11 SADPs showing the three distinct ORs found for C14 precipitates in the A2 solid solution for the sample heat-treated at 1,500 °C for 200 h: **a** OR10, $\mathbf{B} = [\bar{1}2\bar{1}\bar{1}]_{C14}//[1\bar{1}0]_{A2}$; **b** OR11, $\mathbf{B} = [1\bar{1}00]_{C14}//[1\bar{1}0]_{A2}$; **c** OR12, $\mathbf{B} = [11\bar{2}0]_{C14}//[1\bar{1}3]_{A2}$

Table 3 Compositions of the phases in the microstructure after heat treatment at 1,500 °C

Phase	Composition (at.%)				
	Nb	Mo	Cr	Al	Si
A2	31.3	51.5	12.2	4.4	0.5
A15	28.4	41.0	9.2	13.7	7.7
C14	31.0	10.0	42.8	3.7	12.5
Unknown phase (II)	2.2	2.0	0.6	92.0	3.2

the A15 and C14 phases in the eutectic regions and the corresponding precipitates within the A2 phase. This suggests that the phases have reached their equilibrium compositions by diffusional processes during the heat treatment.

Discussion

Solidification microstructure

To the authors' knowledge there is no published quinternary Nb–Mo–Cr–Si–Al equilibrium phase diagram, but the microstructure of the as-cast samples clearly indicates that the alloy solidifies by the formation of A2 dendrites, followed by interdendritic solidification of a eutectic A15/C14 mixture. The persistence of these phases as the main constituents of the heat-treated microstructures, even for temperatures of 1,500 °C, confirms that these are the main equilibrium phases in the alloy. The EDXS data obtained from the as-cast samples show that there is little difference in the Nb contents of the three phases: the A2 phase is Mo-rich and Cr,Si-lean; the A15 phase is Mo-rich and Cr-lean; and the C14 phase is Cr-rich and Mo-lean. It is interesting to note that this three-phase mixture differs from the majority of the in situ composites considered by other authors, for which the ductile primary phase is one of the components of the eutectic phase mixture (the main exception is the formation of Mo plus Mo_3Si–Mo_5SiB_2 eutectics in Mo–Si–B alloys [42–44]). This has obvious implications for the mechanical behavior of the alloy: these issues and the relationship to the atomic site occupancies in the phases are discussed elsewhere [48].

The lamellar morphology adopted by the A15/C14 colonies is consistent with the roughly equal proportions of the phases in the eutectic mixture. Simple geometric

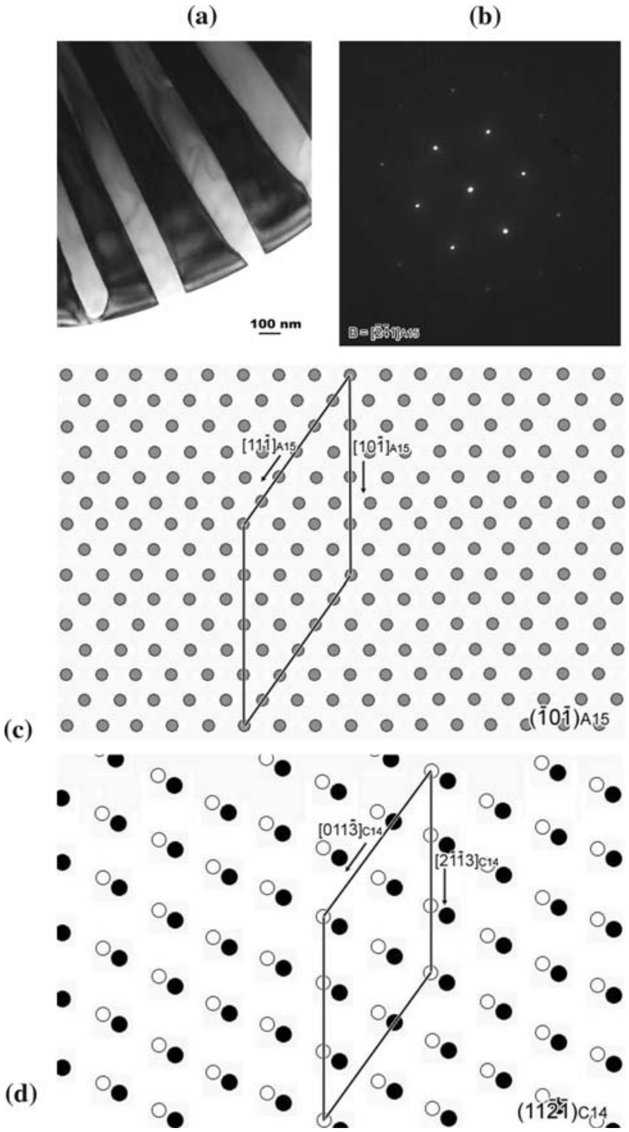

Fig. 12 Coincident site lattice analysis of the interfaces in a eutectic A15/C14 colony, **a** BF TEM image of the colony showing flat parallel interfaces; **b** SADP obtained from the A15 phase in the colony with the interfaces "edge-on"; **c** and **d** Atomic arrangements on the interfaces for the A15/C14 eutectic colony, showing repeat units with parallel translation vectors and having very low misfits

analyses were performed on the lattice points in the largest interfacial facets of several different eutectic colonies. In each of these facets a low-misfit constrained coincident site lattice (CCSL) could be identified. For example, in the colony shown in Fig. 12a the phases adopted OR1 and the interfaces lay nearly parallel to $(101)_{A15}$ and $(11\bar{2}\bar{1})_{C14}$. Now for a colony with OR1 the low-index translation vectors $[10\bar{1}]_{A15}$ and $[11\bar{1}]_{A15}$ in $(101)_{A15}$ lie parallel to $[2\bar{1}\bar{1}3]_{C14}$ and $[01\bar{1}3]_{C14}$ in $(11\bar{2}\bar{1})_{C14}$. Thus, one can define the parallelogram shown in Fig. 12c and d as the repeat unit for a CCSL. The formation of the CCSL would require constraints of −1.72% along $[10\bar{1}]_{A15}$, matching $[2\bar{1}\bar{1}3]_{C14}$ with $4[10\bar{1}]_{A15}$, and −0.26% along $[11\bar{1}]_{A15}$, matching $[01\bar{1}3]_{C14}$ with $3[11\bar{1}]_{A15}$. The sign of the constraint implies a compressive strain in the A15 phase along both directions. Similar CCSLs were identified in all the large interfacial facets studied, and these presumably correspond to the formation of favorable low-energy interfaces.

We note that while a strong correlation has been established between low-order CSLs and low-energy "special" interfaces in cubic materials a variety of other factors must be considered, particularly when dealing with boundaries non-cubic crystals or heterophase interfaces for which few exact CSLs occur (e.g. [52–58]). In the present case where both the order of the CSL and the constraint values are high, it seems unlikely that the formation of such CCSLs is the main reason why the eutectic colonies adopt the observed ORs, and a different explanation for this is proposed in section "Orientation relationships in as-cast eutectic colonies."

Precipitation in samples heat-treated at 1,000 °C

The formation of precipitates within the A2 phase during heat treatment at 1,000 °C presumably occurs because the equilibrium composition at this temperature is different from that of the phase formed during solidification. The EDXS data in Table 2 show that the remaining A2 phase after 100–200 h at 1,000 °C is significantly leaner in Al, Si, and Cr than the primary phase in the as-cast microstructure. Thus, the super-saturation of these elements may provide the driving force for the nucleation of precipitation. The presence of an A15 layer around the A2 dendrites, and large composite laths with A15 cores, indicates that the A15 phase precipitates first. The A15 cores of the A15/C15 composite laths are enriched in Al and Si, and the ORs that they adopt with respect to the surrounding A2 phase are distributed around OR7 and OR8. This variation in the precipitate orientation is rather different from the well-defined ORs exhibited by the other phases in this alloy, but we note that diverse orientation relationships between A15 and A2 (or B2) phases have been noted in other systems. For example, Rong and Aindow [59] showed that the many different ORs that have been reported in Nb–Al–(Ti,V) alloys are clustered into groups, and that these groups are centered around the ORs one would expect for coherent A15 precipitates on the basis of elastic anisotropy. Since OR7 and OR8 lie close to the minima identified in the analysis of Rong and Aindow, similar factors may be responsible.

While the precipitation of A15 phase would reduce the supersaturation of Al and Si within the A2 matrix, it would increase the supersaturation of Cr; this could explain the formation of a Laves phase sheath around the A15 precipitates. The most interesting feature of these composite precipitates is the fact that the material in the sheath exhibits the cubic C15 structure, rather than the equilibrium hexagonal C14 structure exhibited by the Laves phase in the eutectic mixture. This is all the more remarkable because the chemical compositions of the eutectic C14 phase and the C15 sheath around the A15 precipitates are very similar. A possible explanation is suggested by the configuration of the A15/C15 interface. This interface exhibits large planar facets parallel to $\{001\}$ in both phases and both of the observed ORs would correspond to low-misfit CCSLs. To calculate the misfit we use $a_0 =$ 0.498 nm and 0.698 nm for the A15 and C15 phases, respectively; the latter values are obtained by assuming that $a_0(\mathrm{C15}) = \sqrt{2}\ a_0(\mathrm{C14})$. For the regions with OR5, the misfit between $\langle 110 \rangle_{C15}$ and $2\langle 100 \rangle_{A15}$ is −0.89% (the sign of the misfit implies a tensile elastic strain in the C15 sheath). Similarly, for the regions with OR6, the misfit between $\langle 130 \rangle_{C15}$ and $2\langle 120 \rangle_{A15}$ is −0.89%. Thus the C15 structure may be stabilized by the elastic coherency strains in a manner analogous to the high-pressure transformations observed in other A_2B compounds [60].

Further support for this hypothesis can be seen from the ellipsoidal C15 precipitates that form between the composite laths. These ellipsoidal precipitates exhibit a singular OR (OR9) but no well-defined habit plane. The coherency strains can, however, still be estimated from the lattice mismatches along low-index directions. For example, the direction $[1\bar{1}0]_{C15}$ is parallel to $[\bar{1}1\bar{3}]_{A2}$ and the C15 phase would require a 5.5% tensile strain to maintain coherency along this direction, i.e. the same sign as for the C15 sheath on the composite precipitates. Moreover, the defect structure observed in precipitates at the edge of the hole in the TEM samples is reminiscent of those that arise during polymorphic synchroshear transformations in Laves phases [61–63]. Thus, the ellipsoids may adopt the C15 structure as a metastable form during the initial stages of precipitation due to coherency strains; they could then start to transform to the equilibrium C14 phase when the constraint is relaxed at the edge of the TEM sample during thinning.

Precipitation in samples heat-treated at 1,500 °C

The main microstructural changes observed in the samples heat-treated at 1,500 °C are the type of coarsening/spherodization effects that one might expect from diffusional processes at such a high temperature. The details of the precipitation within the A2 phase are, however, more interesting: the A15 precipitates have the same ORs as those in the samples heat-treated at 1,000 °C but have no Laves phase sheath; the Laves phase precipitates exhibit the C14 structure, not C15, and adopt three different well-defined ORs; and there is a very small amount of an Al-rich unknown phase. While the origins of the latter phase are unclear, the A15 and C14 precipitations can be accounted for using an extension of the arguments presented in section "Precipitation in sample heat-treated at 1,000 °C" above.

Let us assume that the precipitates formed in the A2 phase during the initial stages of heat treatment at 1,500 °C are the same as those formed at 1,000 °C, i.e. composite A15/C15 laths exhibiting ORs around OR7 and OR8 with respect to the surrounding A2 phase, and C15 ellipsoids exhibiting OR9. With increasing heat-treatment time, one would expect diffusional processes to lead to a coarsening of both types of precipitates; this would be accompanied by the elimination of the C15 sheath around the composite particles due to the diffusion of Cr from the sheath to the Laves phase precipitates. At some point, the strain energy associated with the formation of coherent metastable C15 particles would exceed that required to initiate plastic relaxation and, as discussed in section "Precipitation in sample heat-treated at 1,000 °C" above, this would lead to the onset of a transformation to the equilibrium C14 structure. This C15/C14 polymorphic transformation has been studied extensively in various Laves phases and is known to occur by synchro-shear processes in which coupled synchro-Shockley partial dislocations give a net shear parallel to $\langle \bar{2}11 \rangle$ on $\{111\}$ [62, 63]. The resultant C14 phase adopts the following orientation relationship with respect to the parent C15 phase:

OR13: $\langle \bar{1}10 \rangle_{C15} // \langle 11\bar{2}0 \rangle_{C14}$, $\{111\}_{C15} // (0001)_{C14}$.

While there are 24 different variants of the $\langle \bar{2}11 \rangle \{111\}$ synchro-shear system, the six different $\langle \bar{2}11 \rangle$ shears on any particular $\{111\}$ give crystallographically equivalent products. As such, there are only four crystallographically distinct ways in which a given C15 precipitate can transform to the C14 structure. Thus, a C15 precipitate with OR9 that transforms to the C14 structure via one of the variants of OR13 will adopt one of four possible resultant C14/A2 ORs given by:

$[1\bar{1}00]_{C14} // [\bar{1}\bar{1}1]_{A2}$, $(0001)_{C14} // (101)_{A2}$
$[11\bar{2}0]_{C14} // [111]_{A2}$, $(0001)_{C14} // (\bar{2}11)_{A2}$
$[11\bar{2}0]_{C14} // [1\bar{1}3]_{A2}$, $(0001)_{C14} // (141)_{A2}$
$[11\bar{2}0]_{C14} // [111]_{A2}$, $(0001)_{C14} // (\bar{1}\bar{2}3)_{A2}$

Of these, the first three ORs have been observed experimentally in this study as OR10, OR11, and OR12, respectively. This supports the premise that the C14 precipitates observed in these samples adopted the C15 structure with OR9 in the initial stages of heat treatment at 1,500 °C.

Orientation relationships in the as-cast eutectic colonies

Following the arguments presented in section "Precipitation in sample heat-treated at 1,500 °C" above, it is tempting to speculate that similar processes might be responsible for the diversity of ORs observed between the C14 and A15 phases in the eutectic colonies of the as-cast microstructure. Thus, the eutectic may form initially by the co-operative nucleation of A15 and C15 phases, and the latter phase would transform to the hexagonal C14 structure during subsequent growth. In this study two low-misfit ORs have been found between A15 and C15 phases: OR5 and OR6. However, when these are combined with OR13 to define the resultant A15/C14 ORs, none of the variants match any of the eutectic ORs measured experimentally.

A crystallographic analysis was performed to identify other possible combinations of ORs and two likely candidates were found. In the first case, the A15 and C15 phases adopt:

OR14: $[\bar{2}\bar{1}0]_{C15}//[03\bar{1}]_{A15}$, $[011]_{C15}//[001]_{A15}$

While this is not equivalent to OR5 or OR6, the misfits are identical, i.e. −0.89% parallel to the directions quoted. If eutectic colonies nucleated with OR14, and the C15 phase then transformed into the equilibrium C14 structure via OR13, then only four crystallographically distinct A15/C14 ORs would result:

$[001]_{A15}//[\bar{2}20\bar{3}]_{C14}$, $(\bar{1}3\bar{5})_{A15}//(0001)_{C14}$
$[001]_{A15}//[\bar{2}20\bar{3}]_{C14}$, $(\bar{2}35)_{A15}//(0001)_{C14}$
$[001]_{A15}//[\bar{1}2\bar{1}0]_{C14}$, $(\bar{3}10)_{A15}//(0001)_{C14}$
$[001]_{A15}//[\bar{1}2\bar{1}0]_{C14}$, $(340)_{A15}//(0001)_{C14}$

Of these four ORs, the first three have been observed experimentally for as-cast eutectic colonies, and these correspond to OR1, OR2, and OR3, respectively.

In the second case, the A15 and C15 phases adopt:

OR15: $[\bar{1}00]_{C15}//[\bar{1}10]_{A15}$, $[011]_{C15}//[001]_{A15}$

Here again, the misfits are −0.89% parallel to the directions quoted, but in this case combining with OR13 gives only two crystallographically distinct A15/C14 ORs:

$[001]_{A15}//[\bar{2}20\bar{3}]_{C14}$, $(\bar{1}12)_{A15}//(0001)_{C14}$
$[001]_{A15}//[\bar{1}2\bar{1}0]_{C14}$, $(\bar{1}\bar{5}0)_{A15}//(0001)_{C14}$

The first of these corresponds to OR4 measured from as-cast eutectic colonies. Thus, although no direct evidence for the initial formation of C15/A15 eutectic colonies has been obtained, nor have regions with OR14 or OR15 been observed experimentally, this could explain the diversity of ORs exhibited by the eutectic colonies.

Conclusions

The microstructures exhibited by an alloy with composition Nb–27Mo–27Cr–9Al–9Si (in at.%) were characterized by X-ray diffraction and electron microscopy techniques. The as-cast alloy comprised a primary dendritic A2 solid solution surrounded by a eutectic mixture of A15 and C14 phases. Heat treatment at 1,000 °C led to extensive precipitation within the A2 phase but there were no significant changes in the eutectic. Three types of nano-scale precipitates were found within the A2 dendrites: A15/C15 composite laths, C15 ellipsoids, and an unknown cubic phase. Heat treatment at 1,500 °C led to the formation of coarser blocky A15 and C14 precipitates within the A2 phase along with a very small amount of an unknown Al-rich phase: there was also extensive coarsening/spherodization of the eutectic mixture.

From the defect structures and ORs exhibited by the phases, it was inferred that the Laves phase in the precipitates formed at 1,000 °C adopts the C15 structure due to tensile coherency stresses; this transforms to the equilibrium C14 structure by synchroshear processes on {111} when the stresses are relaxed. It was proposed that a similar sequence might explain the diversity of ORs exhibited by the eutectic colonies.

Acknowledgements The authors are grateful to Dr. Dilip M. Shah at Pratt & Whitney for providing us with the alloy samples, and to Dr. Richard McLaughlin at Oxford Instruments for assistance with the EBSD experiments.

References

1. Liu CT (1995) Mater Chem Phys 42:77
2. Clemens H, Kestler H (2000) Adv Eng Mater 2:551
3. Lasalmonie A (2006) Intermetallics 14:1123
4. Aindow M, Shyue J, Gaspar TA, Fraser HL (1991) Philos Mag Lett 64:59
5. Hanada S, Murayama Y, Abe Y (1994) Intermetallics 2:155
6. Hanada S (1997) Curr Opin Solid State Mater Sci 2:279
7. Kim HS, Kum D, Hanada S (2000) J Mater Sci 35:235. doi: 10.1023/A:1004737926209
8. Takasugi T, Hanada S, Yoshida M (1995) Mater Sci Eng A 192/193:805
9. Ohta T, Nakagawa Y, Kaneno Y (2003) J Mater Sci 38:657. doi: 10.1023/A:1021807519728
10. Kazantzis AV, Aindow M, Jones IP, Triantafyllidis GK, De Hosson JTM (2007) Acta Mater 55:1873
11. Kazantzis AV, Aindow M, Triantafyllidis GK, De Hosson JTM (2008) Scr Mater 59:788
12. Meyer M, Kramer M, Akinc M (1996) Adv Mater 8:85
13. Chu F, Thoma DJ, McClellan KJ, Peralta P (1999) Mater Sci Eng A 261:44
14. Shah DM, Anton DL, Pope DP, Chin S (1995) Mater Sci Eng A 192/193:658
15. Johnson DR (1999) Curr Opin Solid State Mater Sci 4:249
16. Bewlay BP, Jackson MR, Zhao JC, Subramanian PR (2003) Metall Mater Trans A 34A:2043
17. Bei H, Pharr GM, George EP (2004) J Mater Sci 39:3975. doi: 10.1023/B:JMSC.0000031479.32138.84
18. Bei H, George EP, Kenik EA, Pharr GM (2003) Acta Mater 51:6241
19. Duan G, Wang HM (2002) J Mater Sci 37:1981. doi: 10.1023/A:1015295014177

20. Henshall GA, Strum MJ, Bewlay BP, Sutliff JA (1997) Metall Mater Trans A 28:2555
21. Bencher CD, Murugesh L, Rao KTV, Ritchie RO (1996) Intermetallics 4:23
22. Tappin DK, Smith LS, Horspool DN, Aindow M (1997) Acta Mater 45:4923
23. Tabaru T, Hanada S (1999) Intermetallics 7:807
24. Rong TS, Horspool DN, Aindow M (2002) Intermetallics 10:1
25. Bewlay BP, Sutliff JA, Jackson MR, Lipsitt HA (1994) Acta Metall Mater 42:2869
26. Chan KS (1996) Metall Mater Trans A 27A:2518
27. Bewlay BP, Jackson MR (1996) J Mater Res 11:1917
28. Kumar KS, Liu CT (1997) Acta Mater 45:3671
29. Kumar KS, Pang L, Horton JA, Liu CT (2003) Intermetallics 11:677
30. Chen KC, Allen SM, Livingston JD (1998) Mater Sci Eng A 242:162
31. Kim WY, Takasugi T (2003) Scr Mater 48:559
32. Nakagawa Y, Ohta T, Kaneno Y, Inoue H, Takasugi T (2004) Metall Mater Trans A 35:3469
33. Kumar KS, Pang L, Liu CT, Horton J, Kenik EA (2000) Acta Mater 48:911
34. Liu CT, Zhu JH, Brady MP, McKamey CG, Pike LM (2000) Intermetallics 8:1119
35. Tien RH, Zhu JH, Liu CT, Walker LR (2005) Intermetallics 13:361
36. Mendiratta MG, Dimiduk DM (1991) Scr Metall Mater 25:237
37. Rigney JD, Lewandowski JJ (1996) Metall Mater Trans A 27A:3292
38. Bewlay BP, Jackson MR, Lipsitt HA (1996) Metall Mater Trans A 27:3801
39. Kim WY, Tanaka H, Hanada S (2002) J Mater Sci 37:2885. doi:10.1023/A:1016088107995
40. Ma CL, Li JG, Tan Y, Tanaka R, Hanada S (2004) Mater Sci Eng A 386:375
41. Geng J, Tsakiropoulos P, Shao G (2007) Intermetallics 15:270
42. Schneibel JH, Ritchie RO, Kruzic JJ, Tortorelli PF (2005) Metall Mater Trans A 6:525
43. Yang Y, Chang YA, Tan L, Cao W (2005) Acta Mater 53:1711
44. Sakidja R, Perepezko JH (2007) J Nucl Mater 366:407
45. Brady MP, Liu CT, Zhu JH, Tortorelli PF, Walker LR (2005) Scr Mater 52:815
46. Takasugi T, Yoshida M, Hanada S (1996) Acta Mater 44:669
47. Brady MP, Gleeson B, Wright IG (2001) JOM 1:16
48. Hu Y-L, Zhang LC, Shuman D, Huey BD, Aindow M (2009) Scr Mater 60 (in press)
49. Cullity BD, Stock SR (2001) Elements of X-Ray diffraction, 3rd edn. Prentice-Hall, New Jersey
50. Rabkin E (2005) J Mater Sci 40:875. doi:10.1007/s10853-005-6504-5
51. Rong TS, Smith LS, Aindow M, Jones IP, Loretto MH (2000) Philos Mag Lett 80:519
52. MacLaren I, Aindow M (1997) Philos Mag Lett 76:25
53. Wang YG, Zhang Z, Yan GH, De Hosson JTM (2002) J Mater Sci 37:2511. doi:10.1023/A:1015439624193
54. Zhang LC, Aindow M (2006) J Mater Sci 41:611. doi:10.1007/s10853-006-6477-z
55. Cahn JW, Taylor JE (2006) J Mater Sci 41:7669. doi:10.1007/s10853-006-0592-8
56. King AH, Shekhar S (2006) J Mater Sci 41:7675. doi:10.1007/s10853-006-0665-8
57. Bendersky LA, Cahn JW (2006) J Mater Sci 41:7683. doi:10.1007/s10853-006-0625-3
58. Ranganathan S, Srivastava AK, Lord EA (2006) J Mater Sci 41:7696. doi:10.1007/s10853-006-0966-y
59. Rong TS, Aindow M (1999) Philos Mag Lett 79:93
60. Shekar NVC, Sahu PC (2006) J Mater Sci 41:3207. doi:10.1007/s10853-006-5562-7
61. Liu Y, Livingston JD, Allen SM (1992) Metall Trans A 23:3303
62. Chisholm MF, Kumar S, Hazzledine PM (2005) Science 307:701
63. Kumar KS, Hazzledine PM (2004) Intermetallics 12:763